Numerical study of Risken–Nummedal–Graham–Haken instability in mid-infrared Fabry–Pérot quantum cascade lasers

N. Vukovic[1] · J. Radovanovic[1] · V. Milanovic[1] · D. L. Boiko[2]

Abstract

We review our recent theoretical studies on multimode instabilities in Fabry–Pérot cavity mid-infrared quantum cascade lasers (QCLs) caused by parametric excitation of Rabi flopping oscillations. Numerical simulations are based on the semiclassical traveling wave Maxwell–Bloch equations. QCLs with a few mm cavity without an absorber exhibit intermittent RNGH self-pulsations, while regular self-pulsations are possible in short-cavity QCLs, with the cavity length of 100 μm or smaller. However, the second threshold in short-cavity QCLs is significantly increased compared to the values for a few mm long devices. We provide here a new insight on RNGH instability via bifurcation analysis of the output waveform and studies of the recurrence period density entropy. We propose an interpretation of the broadening/narrowing of the optical spectrum of a QCL i.e. switching the RNGH instability on and off observed in experiment.

Keywords Quantum cascade laser · Self-pulsations · Spatial hole burning · RNGH instability · Bifurcation diagram

✉ N. Vukovic
nvukovic@etf.bg.ac.rs

D. L. Boiko
dmitri.boiko@csem.ch

[1] School of Electrical Engineering, University of Belgrade, Bulevar kralja Aleksandra 73, Belgrade 11120, Serbia

[2] Centre Suisse d'Électronique et de Microtechnique (CSEM), Jaquet-Droz 1, 2002 Neuchâtel, Switzerland

1 Introduction

Periodic pulse production regimes such as self-Q-switching, self-pulsations or passive mode-locking (PML) in interband semiconductor laser diodes (LDs) are widely used in various practical applications. However, these passive regimes are impossible in the mid-infrared (Mid-IR) Quantum Cascade Lasers (QCLs) because of their picosecond (or sub-picosecond) gain recovery time. This time is too short in comparison with the cavity round trip time so the gain saturation does not provide a "memory" mechanism to sustain such periodic regimes (Gordon et al. 2008; Wang et al. 2007). At the same time, the multi-mode Risken–Nummedal–Graham–Haken (RNGH) instability (Graham and Haken 1968; Risken and Nummedal 1968) in QCLs with Fabry–Pérot (FP) cavities (Gordon et al. 2008; Wang et al. 2007) may pave a way to practical approaches for ultrafast pulse production in the Mid-IR range. More specifically, the spatial hole burning (SHB) effect in FP QCLs strongly reduces the excitation threshold for RNGH self-pulsations (SPs).

The question of the origin of RNGH SPs itself is a highly debated subject (Gordon et al. 2008; Mansuripur et al. 2016; Piccardo et al. 2018; Vukovic et al. 2016a, 2017). Strong spectral broadening in single-section FP cavity QCLs (~ 20–60 cm^{-1}) was observed both in the ridge waveguide and in the buried heterostructure design operating under CW or quasi-CW driving conditions just above the lasing threshold (Bugajski et al. 2013; Gordon et al. 2008; Mansuripur et al. 2016; Wang et al. 2007). Low threshold RNGH multimode instability was attributed to a combined effect of spatial hole burning and saturable absorption in the QCL cavity (Gordon et al. 2008) but the nature of saturable absorption which should be equally strong in a ridge waveguide and a buried heterostructure QCLs has never been fully clarified.

Another mechanism of instability in single-section QCLs has been proposed in Mansuripur et al. (2016) and Piccardo et al. (2018), where it was linked to a parametric four-wave mixing gain instability, in full analogy with the phase-locked comb production in high-finesse optically pumped micro-cavities (Herr et al. 2014) The idea stems from a parametric gain picture yielding instability of the main cavity mode, along the line of comb generation in optically pumped dielectric microdisk resonators with third-order $\chi^{(3)}$ non-linearity. Mid-IR intersubband transitions in semiconductor QWs do produce strong third-order nonlinearity (Capasso et al. 1994; Gravé et al. 1992). However, optically passive microdisk resonators have a special cavity design to achieve a very high-quality factor ($Q \sim 10^8$). In order to reach parametric instability threshold, they employ whispering gallery modes with very small transverse sizes and operate with circulating pump power in the resonator on the order of several hundreds of watts. Electrically pumped Mid-IR QCLs with FP cavities cannot reproduce such environment to reach a parametric instability caused by material third-order nonlinearity $\chi^{(3)}$. This conjecture is in agreement with the fact that all measurements of the second-order interferometric autocorrelation (IAC) traces reported for FP cavity QCLs reveal the peak to background ratio close to 8:3, which corresponds to a noisy multimode lasing as opposed to the ratio of 8:1 for a perfectly phase-locked comb (Diels and Rudolph 2006).

In our theoretical studies (Vukovic et al. 2016a, b, 2017) on the RNGH instability in QCLs we attribute the leading role to the gratings of population inversion and coherences (medium polarization) induced by the standing wave pattern of the cavity modes due to the spatial hole burning (SHB) effect. The formation of the carrier and coherence gratings is conditioned by the carrier lifetime T_1 (longitudinal relaxation time), the carrier dephasing time T_2 (transverse relaxation time) and the carrier diffusion coefficient D.

2 Model

The starting point of our analysis is the system of Maxwell–Bloch equations (Vukovic et al. 2016b, 2017):

$$\dot{\rho}_{ab} = i\omega\rho_{ab} + i\frac{\mu E}{\hbar}\Delta - \frac{\rho_{ab}}{T_2} + D\frac{\partial^2\rho_{ab}}{\partial z^2} \tag{1}$$

$$\dot{\Delta} = -2i\frac{\mu E}{\hbar}(\rho_{ab}^* - \rho_{ab}) + \frac{\Delta_{pump} - \Delta}{T_1} + D\frac{\partial^2\Delta}{\partial z^2} \tag{2}$$

$$\partial_z^2 E - \frac{n_g^2}{c^2}\partial_t^2 E = \Gamma\frac{N\mu}{\varepsilon_0 c^2}\partial_t^2(\rho_{ab}^* + \rho_{ab}) + \frac{n_g l_0'}{c}\partial_t E \tag{3}$$

where ρ_{ab} is the off-diagonal element of the density matrix, $\Delta = \rho_{bb} - \rho_{aa}$ is the population inversion, ω, and μ denote the resonant frequency and the dipole matrix element respectively. Δ_{pump} is the steady-state population inversion, E, N, and Γ stand for the optical field, the number of two-level systems per unit volume and the overlap factor between the optical mode and the active region, n_g is the group refractive index (Vukovic et al. 2016a, b, 2017). Numerical simulations with the semiclassical traveling wave (TW) rate equation model (Vukovic et al. 2016a, 2017) are accomplished by introducing in Eqs. (1)–(3) two slowly varying amplitudes for the counter-propagating waves in the FP cavity $A_{\pm}$ and distinguishing the medium's polarizations associated with the forward and backward traveling waves $P_{\pm}$ (Boiko and Vasil'ev 2012):

$$\frac{\partial A_{\pm}}{\partial t} \pm \frac{c}{n_g}\frac{\partial A_{\pm}}{\partial z} = \frac{1}{2}\Gamma\sqrt{\frac{g_0}{T_2}}P_{\pm} - \frac{1}{2}\frac{c}{n_g}\alpha_i A_{\pm} \tag{4}$$

$$\frac{\partial P_{\pm}}{\partial t} = -\frac{P_{\pm}}{T_2} + \sqrt{\frac{g_0}{T_2}}(n - n_t)A_{\pm} + D\frac{\partial^2 P_{\pm}}{\partial z^2} + \Lambda_{\pm}, \tag{5}$$

$$\frac{\partial n}{\partial t} = -\frac{n}{\tau_n} - \sqrt{\frac{g_0}{T_2}}(A_+ P_+ + A_- P_-) + \frac{J(z,t)}{ed} + D\frac{\partial^2 n}{\partial z^2}. \tag{6}$$

Here, $J(z,t)$ is pump current density and d is the active region thickness. The model is adapted from Boiko and Vasil'ev (2012) by removing the saturable absorber section. It incorporates Langevin force terms $\Lambda_{\pm}$ in Eq. (5) that seed spontaneous polarization noise into the system. The QCL gain chip parameters used in numerical simulations are listed in Table 1.

The field amplitudes are normalized in accordance with the secondary quantization convention $\hat{a}_{\pm}|N_{\pm}\rangle = A_{\pm}|N_{\pm} - 1\rangle$:

$$E_{\pm} = \sqrt{\frac{4\pi\hbar\omega}{n_g^2}}e_{\pm}A_{\pm}\sin(\omega t \mp kz), \quad A_{\pm} = \sqrt{N_{\pm}} \tag{7}$$

The medium's polarization (the ensemble average for the off-diagonal elements of the density matrix) is normalized as follows:

Table 1 Dynamic model parameters for InGaAs QCL considered in this paper using data from Vukovic et al. (2016a, b, 2017)

Symbol	Quantity	Value
λ	Lasing wavelength	10 μm
T_1	Carrier lifetime	1.3 ps[a] or 0.5 ps[b]
T_2	Carrier dephasing time	140 fs
α_i	Intrinsic material loss	24 cm^{-1}
D	Diffusion coefficient	180 cm^2/s
n_g	Group refractive index	3.3
R_1	QCL back facet reflectivity	27%
R_2	QCL front facet reflectivity	27%
Γ	Optical mode confinement factor	0.55
$g_0 = \partial g / \partial n$	Differential gain of one cascade	2.1×10^{-4} cm^3/s
n_t	Transparency carrier density	7×10^{14} cm^{-3}

[a]Figures 1, 2 and 3

[b]Figures 4, 5 and 6

$$P_\pm = \sqrt{\frac{n_g^2 g_0}{4\pi\omega T_2}} \, e_\pm P_\pm \sin(\omega t \mp kz). \tag{8}$$

Boundary conditions for the wave amplitudes are applied at left ($z=0$) and right ($z=L$) cavity facets in the usual way:

$$A_+(0,t) = \sqrt{R_1} A_-(0,t),$$
$$A_-(L,t) = \sqrt{R_2} A_+(L,t). \tag{9}$$

The evolution of the carrier density n, medium polarization $P_\pm$ (coherences) and output power at the facets is obtained by numerically integrating the system of Eqs. (4)–(9) (Boiko and Vasil'ev 2012).

3 Results and discussion

3.1 Short cavity FP QCLs

To begin with, we consider an FP QCL chip with a very short cavity ($L=0.1$ mm) and $T_1=1.3$ ps. Excitation of RNGH self-pulsation regime requires a perturbation which is achieved by introducing polarization noise in the model (Langevin force terms in Eq. (5)). The cavity round trip time ($T_{cav}=2.2$ ps) is comparable to the gain recovery time and QCL produces regular RNGH self-pulsations at a current of $p_{th2}=2.4$ times above the lasing threshold (Vukovic et al. 2016a, b, 2017). Numerical simulations reveal the onset of self-pulsations within the first 8 ps interval (~4 cavity round trips). After 30 ps (~14 cavity round trips), we observe a transit to a steady regime of regular self-pulsations (Vukovic et al. 2017). The waveform example can be found in the inset of Fig. 1a. The field has a sine-wave envelope with a period being close to the cavity round trip time of 2.2 ps. The optical field and polarization of the gain medium change the sign at each passage in the cavity (at each half-period of the sine-wave). The intensity pulses are of 0.9 THz repetition
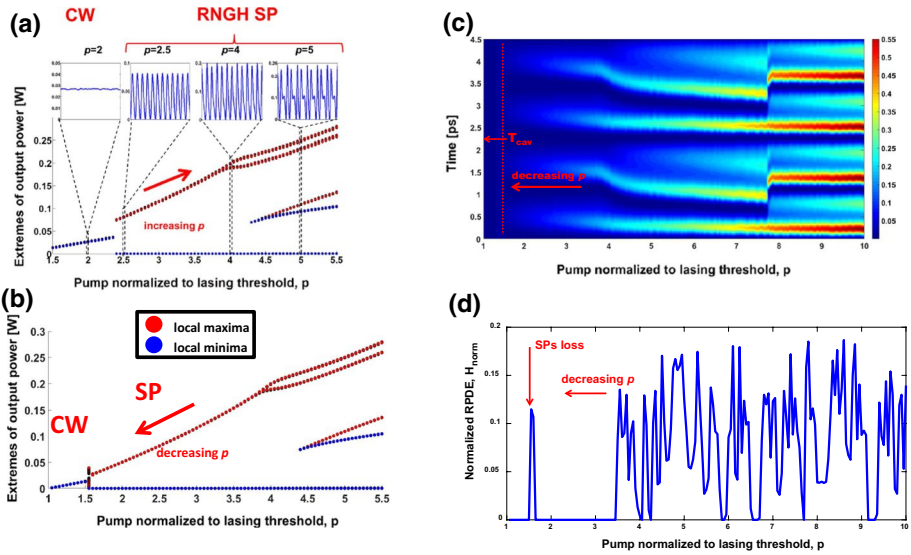
Fig. 1 Results of numerical simulations with TW model for monolithic QCL of the cavity length 100 μm: **a** bifurcation diagrams of self-starting SPs represented by extreme values in the output power waveform P_{out} (red and blue symbols correspond to the maxima and minima, respectively). The insets show the steady-state P_{out} waveforms for different p values. **b** Bifurcation diagram of stable SPs (but not necessarily self-starting) obtained by adiabatically decreasing p from the initial value of $p = 5.5$. Note a bi-stability region $p = 1.55$–2.4 in (**a**, **b**). **c** Contour plot of P_{out} distribution when decreasing p (long time scale, x-axis), during time interval equal to 2 cavity round trips (short time scale, y-axis). **d** Behavior of the normalized Recurrence Period Density Entropy (RPDE) (Little et al. 2007) with decreasing p. The following time-embedding parameters are used: embedding dimension $m = 4$, embedding delay $\tau = 10$, embedding ball radius r = 0.003. More details about these parameters can be found in Kantz and Schreiber (2004) and Little et al. (2007). (Color figure online)

rate and of 0.6 ps FWHM duration. The examples of optical and RF power spectra, 2nd order IAC traces as well as P-N attractors can be found in Vukovic et al. (2016a, b, 2017).

In contrast to our previous studies focused at the origin of the RNGH SPs (Vukovic et al. 2016a, b, 2017), in this paper we analyze bifurcations of the self-pulsations waveform as a function of the pump current, which we normalize to the lasing threshold $p = I/I_{th}$. We construct the bifurcation diagrams in a few different ways. In all cases, the pump current is changed in small steps of $\delta p = 0.05$. For each p value, the numerical simulations are performed over 50 cavity round trips while only the last 25 periods after the end of all transients are used in the waveform analysis.

The bifurcation diagrams of extreme values (maxima and minima) in the output power waveform P_{out} are plotted in Fig. 1a, b. The red (blue) circles indicate the global and local maxima (minima) in the output power waveform. For instance, the largest values designate the peak power variations while the zero values in the output power waveform are due to the sign changes in the optical field envelope.

In Fig. 1a, for each value of p, we reset the initial conditions to zero field and let the self-pulsations to occur and grow. Thus we obtain the bifurcation diagram of the self-starting SPs. For example, for p above the second threshold $p_{th2} = 2.4$, the QCL exhibits a self-starting oscillatory behavior, while below p_{th2}, it exhibits only CW emission. The insets

in Fig. 1a display the corresponding output power waveforms for different pump rates and provide a hint for interpretation of the bifurcation diagram.

In the bifurcation diagram of Fig. 1b, we study the stability of already ongoing SPs which have been excited earlier. In a particular case, we start the numerical simulations from the largest value of $p = 5.5$ to excite the SPs. After that, we adiabatically reduce the pump current in small δp steps. In contrast to the sequence used in Fig. 1a, for each value of p, we continue the simulations without resetting the initial conditions to zero field. Surprisingly, for the adiabatically decreasing pump rate, the SPs continue even below the self-excitation threshold p_{th2}. There is thus a hysteresis loop, associated with a bi-stable QCL operation either in the RNGH SPs or CW lasing regimes in the range from $p = 1.5$–2.4 [compare Fig. 1a, b]. This hysteresis loop effect is in agreement with the results of Lyapunov stability analysis and RNGH threshold discussed in Vukovic et al. (2016a, 2017). For $p > p_{min}$, the Lyapunov exponent is positive, that is the SPs regime is possible. For instance, $p_{min} \approx 1.3$ was obtained for QCL with parameters shown in Table 1 (Vukovic et al. 2017). However, the self-starting RNGH SPs in a short-cavity QCL can build up provided the initial optical pulse perturbation is of sufficient pulse area. This condition is met at $p > p_{th2}$ ($p_{th2} \approx 2.4$ in considered case). Note that the longer the QCL cavity, the smaller the hysteresis width. In mm-long QCL devices, the hysteresis loop practically disappears because of $p_{th2} \approx p_{min}$ (Vukovic et al. 2016a, 2017).

With increasing pump rate p, we observe a period-doubling (at $p = 4$) of intensity SPs and harmonic waveform distortion.

To study whether we can trigger a sequence of the period-doubling and a bifurcation to chaos, we resolve the QCL dynamics on the fast (within one cavity round trip) and the slow (on subsequent cavity round trips) time scales, while adiabatically changing p. In Fig. 1c we show a contour plot representing the evolution of the output power waveform with decreasing p. For $10 > p > 7.8$, the period of intensity SPs is equal to the half of the cavity round trip time. Then for $7.8 > p > 4$, the period-doubling occurs (the period of SP is equal to the round trip time). For $p < 4$, the period of intensity SPs reduces back to the half of the cavity round trip time. We thus do not observe any sign of the period-doubling sequence.

In Fig. 1d we calculate the normalized recurrence period density entropy (RPDE) (Little et al. 2007), by applying a so-called time-delay embedding (Kantz and Schreiber 2004). Recall that a perfectly periodic waveform (and a CW signal) has the RPDE entropy value of "0", while the RPDE value of "1" corresponds to chaos. In this manner, the RPDE indicates whether the SPs are periodic or quasi-periodic (chaotic).

For a short-cavity QCL in Fig. 1d, the RPDE entropy oscillates nearby "0" attesting for a perfectly periodic waveform even at a high pump rate p despite strong waveform anharmonicity. The spike on the RPDE curve at the lower p side of the SP/CW hysteresis loop can be attributed to the loss of stability of the SP regime at $p \leq p_{min}$ and, as a consequence, to a higher sensitivity of the waveform to polarization noise $\Lambda_{\pm}$ injected in the model system (Vukovic et al. 2017).

In the considered example of a short-cavity QCL, the optical gain "memory" effect ($T_1 = 1.3$ ps) persists between the subsequent passages in the cavity ($T_{cav}/2 = 1.1$ ps), resulting in a regular pulse train.

3.2 Long cavity FP QCLs

In this subsection, we present numerically calculated optical field waveform, optical and RF power spectra, IAC trace, bifurcation diagram and RPDE plots for 1.5 mm length FP

QCL chip and the same $T_1 = 1.3$ ps as for the short cavity QCL in subsection 3.1. The cavity round-trip time is $T_{cav} = 33$ ps while all other parameters can be found in Table 1. Figure 2a shows the optical field waveform when the pump rate normalized to the lasing threshold is $p = 2$. It develops into square waves, in agreement with our findings in Vukovic et al. (2017). The waveform just slightly changes at each round-trip, yielding the quasi-periodic chaotic behavior. Optical spectra in Fig. 2b shows suppression of the main lasing mode (at 0 GHz) in agreement with multimode behavior observed experimentally (Gordon et al. 2008; Wang et al. 2007) and calculated numerically in Vukovic et al. (2017). RF power spectrum depicted in Fig. 2c confirms multimode comb emission. In Fig. 2d we calculate the interferometric autocorrelation trace. The peak to background ratio of the interferometric AC trace for the numerically simulated output waveform is worse than 8:3, as it can be expected for such noisy multimode lasing behavior (Diels and Rudolph 2006). However it is this 8:3 peak to background ratio that was found in experimentally measured interferometric AC traces (Antonov et al. 2017a, b; Boiko et al. 2017; Gordon et al. 2008). Quasi-periodic chaotic pulse train (Fig. 2a) with multiple pulses on the cavity round-trip is responsible for the secondary lobes seen in the IAC trace in between the cavity round-trips, (Fig. 2d). Similar IAC traces with secondary lobes have been experimentally observed in Gordon et al. 2008. In some
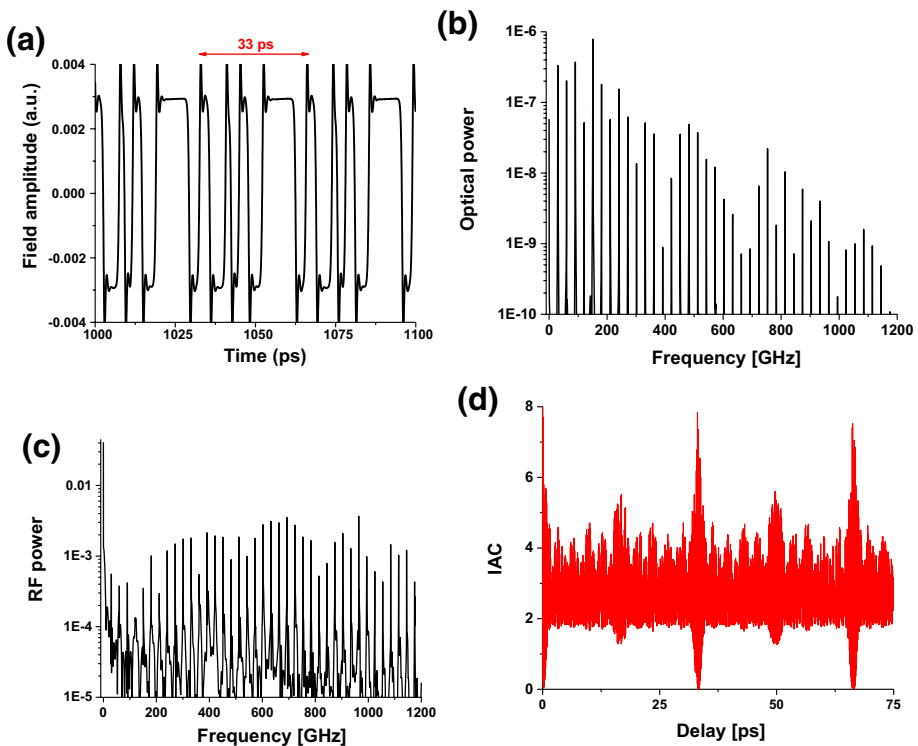
Fig. 2 Results of numerical simulations with TW model for monolithic QCL of the cavity length 1.5 mm ($T_{cav} = 33$ ps): **a** field amplitude waveform. **b** Optical power spectrum. Cavity modes are separated by 30 GHz and only modes with positive detuning from the main lasing mode (at zero frequency) are shown. **c** RF power spectrum. **d** IAC trace. More spectra and attractor plots can be found in Vukovic et al. (2017)

realizations, they appear nearly at half of the cavity round-trip as in Fig. 2d [other examples can be found in Vukovic et al. (2017)].

In Fig. 3a we plot the bifurcation diagram of the waveform intensity extremes and in Fig. 3b we show the RPDE in function of adiabatically increasing pump rate p. SPs start at very low pump excess above threshold ($p_{th2} \sim 1.1$) while the bistable CW/SP region between p_{min} and p_{th2} is very narrow in QCLs with mm-long cavities. In Fig. 3a, for the pump rate higher than $p = 2.5$ the number of local extremes in the intensity waveform increases, as well as their amplitude, the intensity waveform becomes more chaotic.

In Fig. 3b, large values of RPDE entropy (compare to Fig. 1d) attest that the waveform becomes quasi-periodic ($p > 1.2$) or even chaotic ($p > 2.5$) when it reaches 0.7, as we suspected from Fig. 3a and the IAC trace from Fig. 2d for $p = 2$.

3.3 Switching the Risken–Nummedal–Graham–Haken instability on and off

In Antonov et al. (2017a, b) and Boiko et al. (2017) authors have shown experimentally that the onset of broadband multimode emission associated with RNGH instability in the FP cavity QCLs can be tailored during a transient switching-on process under the pulsed pumping. Homogeneous interaction of all cascades (periods) with the lasing mode and a small diffusion length allows for a strong SHB effect and facilitates formation of the population and coherence gratings. It was proposed that in these conditions, a sudden increase of the carrier lifetime T_1 e.g. from 0.2 to 0.5 ps as a result of the lasing transition change causes a drop in the second threshold. A QCL starting initially to operate in the usual emission regime with a few lasing cavity modes switch to broadband multimode RNGH self-pulsations (Antonov et al. 2017a, b).

Fig. 3 Results of numerical simulations with TW model for monolithic QCL of the cavity length 1.5 mm: **a** bifurcation diagrams of self-starting SPs represented by extreme values in the output power waveform P_{out} (red and blue symbols correspond to the maxima and minima, respectively). **b** The behavior of the normalized Recurrence Period Density Entropy (RPDE) (Little et al. 2007) with increasing p. The following time-embedding parameters are used: embedding dimension $m = 4$, embedding delay $\tau = 10$, embedding ball radius r = 0.02. More details about these parameters can be found in Kantz and Schreiber (2004) and Little et al. (2007). (Color figure online)
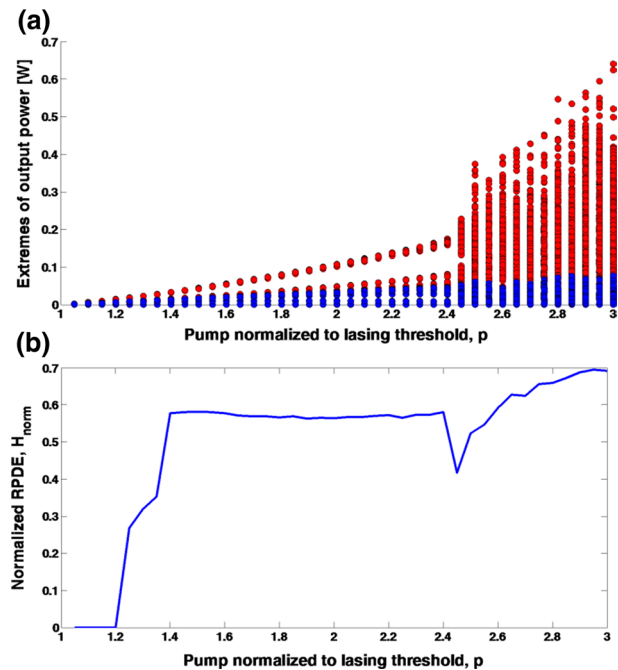
The second mechanism proposed in Antonov et al. (2017a, b) is for the switching-off of the RNGH instability at high currents. It has been attributed to the change of the contrast of the SHB-induced grating as a result of inhomogeneous interaction of the cascades with the lasing field when driving a QCL on the unstable part of I-V curve leads to a formation of electric field domains (EFDs) with non-uniform charge accumulation and depletion across the QCL periods (Lu et al. 2006; Wienold et al. 2011). The contrast reduction of the population grating as a result of inhomogeneous broadening reduces the efficiency of the mode coupling through the induced carrier grating and leads to an increase of the second threshold to prohibitively high currents (Antonov et al. 2017a).

These experimentally observed changes in the dynamic regimes were explained using a simple analytical expression for the second threshold in QCLs (Vukovic et al. 2016a). Here we verify both mechanisms of RNGH instability switching in numerical simulations. As a reference testbed, we use a FP QCL with a very short cavity (L=0.1 mm), $\lambda=8$ μm, $T_1=0.5$ ps, $1/4Dk^2=2$ ps, and all other parameters being as listed in Table 1. We label it as "QCL#1" (The upper state lifetime $T_1=0.5$ ps is more realistic in Mid-IR QCLs). In Fig. 4 we study the evolution of the output intensity waveform in QCL#1 and resolve its dynamics on the fast (within two cavity round trips) and the slow (on subsequent cavity round trips) time scales. In difference to Fig. 1c obtained with adiabatically decreasing pump current, in Fig. 4 the bifurcation map is built for the pump rate increasing adiabatically in small steps of $\delta p=0.05$. Self-starting RNGH self-pulsations occur at a current of $I_{th2}=0.45$ A corresponding to the normalized pump rate of $p_{th2}=2.1$ times above the lasing threshold.

The period of self-starting intensity self-pulsations is equal to the cavity round trip time (2.2 ps). Output power waveform develops into two pulses per round trip, where width of the pulses is approximately equal to T_1.

To verify the suppression of RNGH SPs for a transition with a shorter gain recovery time, we perform a second test. In a model device labeled as QCL#2 we decrease the carrier relaxation time T_1 down to 0.2 ps, and take all other parameters as in the reference QCL#1. The waveform bifurcation diagram for QCL#2 is plotted as a color map in Fig. 5. The pump excess above threshold required to excite RNGH SP increases from $p_{th2}=2.1$ (in QCL#1) to $p_{th2}=2.5$ indicating that RNGH instability is indeed more difficult to achieve if the lasing transition has a very short gain recovery time. This conclusion is in qualitative
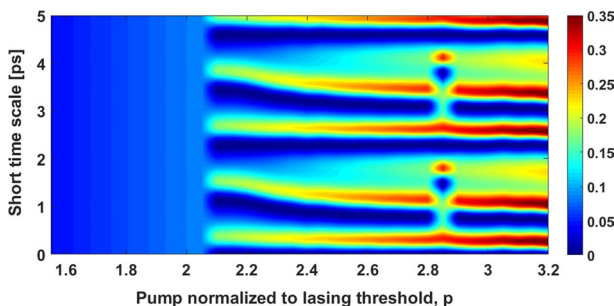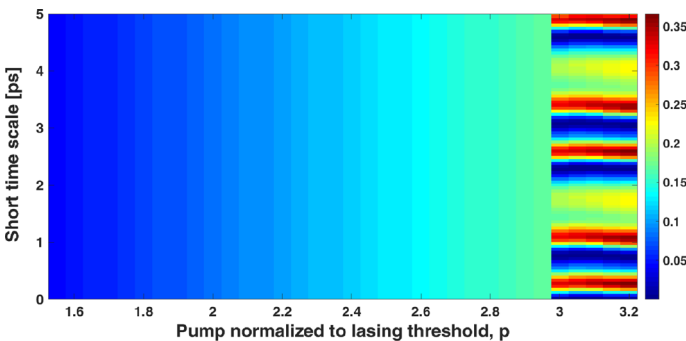

Fig. 4 Numerical simulations with the TW model for monolithic QCL of the cavity length 100 μm, QCL#1. Color map of P_{out} distribution when adiabatically increasing p (long time scale, x-axis), during a time interval equal to 2 cavity round trips (short time scale, y-axis). Carrier relaxation time $T_1=0.5$ ps, carrier decoherence time $T_2=0.14$ ps, diffusion coefficient $D=180$ cm^2/s, the emission wavelength $\lambda=8$ μm. Note that in comparison with Fig. 1c here we increase p while resetting field to zero, and use lower T_1
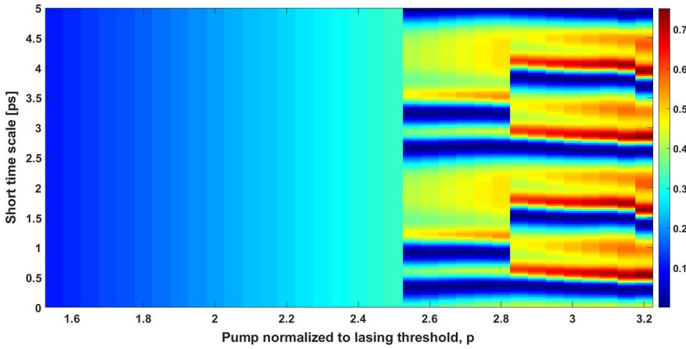
Fig. 5 Numerical simulations with the TW model for monolithic QCL of the cavity length 100 μm, QCL#2. Color map of P_{out} distribution when adiabatically increasing p (long time scale, x-axis), during a time interval equal to 2 cavity round trips (short time scale, y-axis). Carrier relaxation time $T_1 = 0.2$ ps, while all other parameters are the same as in Fig. 4, for QCL#1

agreement with experimental results from Antonov et al. (2017a) showing no RNGH SPs for transient lasing on a transition from an upper subband with reduced carrier lifetime.

The reduction of the SHB is modeled by introducing strong carrier diffusion such that $4Dk^2T_1 \geq 1$. In the third numerical test (QCL#3) we increase the diffusion coefficient D by a factor of 5 (to the value $D = 900$ cm^2/s) in order to make the population grating relaxation time comparable to T_1, i.e. $1/4Dk^2 = 0.4$ ps, while other parameters are the same as in QCL#1. As a result, the contrast of the SHB-induced grating is significantly reduced. The waveform bifurcation diagram for QCL#3 is shown in Fig. 6. The second threshold current increases in 1.4 times as compared to QCL#1 in Fig. 4. This test confirms that RNGH SPs can be suppressed at a high pump rate if SHB strength is reduced. This provides a possible interpretation of the experimental results from Antonov et al. (2017a) and Bugajski et al. (2013) where RNGH SPs cease at high currents. Once QCL bias exceeds the optimal one for the tunneling resonance, QCL enters into the part of the I-V curve characterized by unstable electric field domain formation (EFD) (Lu et al.

Fig. 6 Numerical simulations with the TW model for monolithic QCL of the cavity length 100 μm, QCL#3. Color map of P_{out} distribution when adiabatically increasing p (long time scale, x-axis), during a time interval equal to 2 cavity round trips (short time scale, y-axis). Diffusion coefficient $D = 900$ cm^2/s, while all other parameters are the same as in Fig. 4

2006). It results in inhomogeneous broadening of the gain across different cascades and hence in the weakening of the SHB effect.

4 Summary

In this paper, we provide a review of our recent theoretical studies on the origin of Risken–Nummedal–Graham–Haken self-pulsations and large spectral broadening in mid-infrared FP QCLs. We report new results on bifurcation analysis of the waveforms and the recurrence period density entropy used to distinguish periodic self-pulsations from the chaotic self-pulsations. We provide numerical simulations supporting our interpretation of switching the RNGH self-pulsations on and off observed in the experiment. Our findings open up a new point of view on understanding RNGH instability and the possibility of controlling it for specific applications.

References

Antonov, A.V., Kuritsyn, D.I., Gajic, A., Orlova, E.E., Radovanovic, J., Vaks, V.V., Boiko, D.L.: Switching on and off the Risken–Nummedal–Graham–Haken instability in quantum cascade lasers, pp. 1–31. arXiv Prepr. arXiv:1711.10749 (2017a)

Antonov, A.A., Kuritsyn, D.I., Gajic, A., Orlova, E.E., Radovanovic, J., Vaks, V.V., Boiko, D.L.: Tailoring Risken–Nummedal–Graham–Haken instability in quantum cascade lasers. In: 2017 European Conference on Lasers and Electro-Optics and European Quantum Electronics Conference, p. CC_P_4. Optical Society of America (2017b)

Boiko, D.L., Vasil'ev, P.P.: Superradiance dynamics in semiconductor laser diode structures. Opt. Express **20**, 9501–9515 (2012). https://doi.org/10.1364/oe.20.009501

Boiko, D.L., Antonov, A.V., Kuritsyn, D.I., Yablonskiy, A.N., Sergeev, S.M., Orlova, E.E., Vaks, V.V.: Mid-infrared two photon absorption sensitivity of commercial detectors. Appl. Phys. Lett. **111**, 171102 (2017). https://doi.org/10.1063/1.4996187

Bugajski, M., Pierscinski, K., Pierscinska, D., Szerling, A., Kosiel, K.: Multimode instabilities in mid-infrared quantum cascade lasers. Photonics Lett. Pol. **5**, 85–87 (2013). https://doi.org/10.4302/plp.2013.3.02

Capasso, F., Sirtori, C., Cho, A.Y.: Coupled quantum well semiconductors with giant electric field tunable nonlinear optical properties in the infrared. IEEE J. Quantum Electron. **30**, 1313–1326 (1994). https://doi.org/10.1109/3.303697

Diels, J.-C., Rudolph, W.: Ultrashort Laser Pulse Phenomena: Fundamentals, Techniques, and Applications on a Femtosecond Time Scale. Elsevier, Amsterdam (2006)

Gordon, A., Wang, C.Y., Diehl, L., Kärtner, F.X., Belyanin, A., Bour, D., Corzine, S., Höfler, G., Liu, H.C., Schneider, H., Maier, T., Troccoli, M., Faist, J., Capasso, F.: Multimode regimes in quantum cascade lasers: from coherent instabilities to spatial hole burning. Phys. Rev. A **77**, 053804 (2008). https://doi.org/10.1103/PhysRevA.77.053804

Graham, R., Haken, H.: Quantum theory of light propagation in a fluctuating laser-active medium. Zeitschrift für Phys. **213**, 420–450 (1968). https://doi.org/10.1007/BF01405384

Gravé, I., Segev, M., Yariv, A.: Observation of phase conjugation at 10.6 μm via intersubband third-order nonlinearities in a GaAs/AlGaAs multi-quantum-well structure. Appl. Phys. Lett. **60**, 2717–2719 (1992). https://doi.org/10.1063/1.106854

Herr, T., Brasch, V., Jost, J.D., Wang, C.Y., Kondratiev, N.M., Gorodetsky, M.L., Kippenberg, T.J.: Temporal solitons in optical microresonators. Nat. Photonics **8**, 145–152 (2014). https://doi.org/10.1038/nphoton.2013.343

Kantz, H., Schreiber, T.: Nonlinear Time Series Analysis. Cambridge University Press, Cambridge (2004)

Little, M.A., McSharry, P.E., Roberts, S.J., Costello, D.A.E., Moroz, I.M.: Exploiting nonlinear recurrence and fractal scaling properties for voice disorder detection. Biomed. Eng. Online **6**, 23 (2007). https://doi.org/10.1186/1475-925X-6-23

Lu, S.L., Schrottke, L., Teitsworth, S.W., Hey, R., Grahn, H.T.: Formation of electric-field domains in GaAs/Al$_x$Ga$_{1-x}$As quantum cascade laser structures. Phys. Rev. B **73**, 033311 (2006). https://doi.org/10.1103/PhysRevB.73.033311

Mansuripur, T.S., Vernet, C., Chevalier, P., Aoust, G., Schwarz, B., Xie, F., Caneau, C., Lascola, K., Zah, C., Caffey, D.P., Day, T., Missaggia, L.J., Connors, M.K., Wang, C.A., Belyanin, A., Capasso, F.: Single-mode instability in standing-wave lasers: the quantum cascade laser as a self-pumped parametric oscillator. Phys. Rev. A **94**, 063807 (2016). https://doi.org/10.1103/PhysRevA.94.063807

Piccardo, M., Chevalier, P., Mansuripur, T.S., Kazakov, D., Wang, Y., Rubin, N.A., Meadowcroft, L., Belyanin, A., Capasso, F.: The harmonic state of quantum cascade lasers: origin, control, and prospective applications [Invited]. Opt. Express **26**, 9464–9483 (2018). https://doi.org/10.1364/OE.26.009464

Risken, H., Nummedal, K.: Self-pulsing in lasers. J. Appl. Phys. **39**, 4662–4672 (1968). https://doi.org/10.1063/1.1655817

Vukovic, N., Radovanovic, J., Milanovic, V., Boiko, D.L.: Analytical expression for Risken–Nummedal–Graham–Haken instability threshold in quantum cascade lasers. Opt. Express **24**, 26911–26929 (2016a). https://doi.org/10.1364/oe.24.026911

Vukovic, N., Radovanovic, J., Milanovic, V., Boiko, D.L.: Multimode RNGH instabilities of Fabry–Pérot cavity QCLs: impact of diffusion. Opt. Quantum Electron. **48**, 254 (2016b). https://doi.org/10.1007/s11082-016-0515-0

Vukovic, N.N., Radovanovic, J., Milanovic, V., Boiko, D.L.: Low-threshold RNGH instabilities in quantum cascade lasers. IEEE J. Sel. Top. Quantum Electron. **23**, 1200616 (2017). https://doi.org/10.1109/JSTQE.2017.2699139

Wang, C.Y., Diehl, L., Gordon, A., Jirauschek, C., Kärtner, F.X., Belyanin, A., Bour, D., Corzine, S., Höfler, G., Troccoli, M., Faist, J., Capasso, F.: Coherent instabilities in a semiconductor laser with fast gain recovery. Phys. Rev. A **75**, 031802 (2007). https://doi.org/10.1103/PhysRevA.75.031802

Wienold, M., Schrottke, L., Giehler, M., Hey, R., Grahn, H.T.: Nonlinear transport in quantum-cascade lasers: the role of electric-field domain formation for the laser characteristics. J. Appl. Phys. **109**, 073112 (2011). https://doi.org/10.1063/1.3573504